remote sensing

MDPI

Article

The July/August 2019 Lava Flows at the Sciara del Fuoco, Stromboli–Analysis from Multi-Sensor Infrared Satellite Imagery

Simon Plank [1,*], Francesco Marchese [2], Carolina Filizzola [2], Nicola Pergola [2], Marco Neri [3], Michael Nolde [1] and Sandro Martinis [1]

[1] German Aerospace Center (DLR), German Remote Sensing Data Center (DFD), Muenchener Str. 20, 82234 Oberpfaffenhofen, Germany; michael.nolde@dlr.de (M.N.); sandro.martinis@dlr.de (S.M.)

[2] National Research Council of Italy (CNR), Institute of Methodologies for Environmental Analysis (IMAA), 85050 Tito Scalo, Italy; francesco.marchese@imaa.cnr.it (F.M.); carolina.filizzola@imaa.cnr.it (C.F.); nicola.pergola@imaa.cnr.it (N.P.)

[3] Istituto Nazionale di Geofisica e Vulcanologia, Sezione di Catania, Osservatorio Etneo, Piazza Roma 2, 95125 Catania, Italy; marco.neri@ingv.it

* Correspondence: simon.plank@dlr.de; Tel.: +49-8153-28-3460

Received: 15 November 2019; Accepted: 30 November 2019; Published: 3 December 2019

Abstract: On 3 July 2019 a rapid sequence of paroxysmal explosions at the summit craters of Stromboli (Aeolian-Islands, Italy) occurred, followed by a period of intense Strombolian and effusive activity in July, and continuing until the end of August 2019. We present a joint analysis of multi-sensor infrared satellite imagery to investigate this eruption episode. Data from the Spinning-Enhanced-Visible-and-InfraRed-Imager (SEVIRI) was used in combination with those from the Multispectral-Instrument (MSI), the Operational-Land-Imager (OLI), the Advanced-Very High-Resolution-Radiometer (AVHRR), and the Visible-Infrared-Imaging-Radiometer-Suite (VIIRS). The analysis of infrared SEVIRI-data allowed us to detect eruption onset and to investigate short-term variations of thermal volcanic activity, providing information in agreement with that inferred by nighttime-AVHRR-observations. By using Sentinel-2-MSI and Landsat-8-OLI imagery, we better localized the active lava-flows. The latter were quantitatively characterized using infrared VIIRS-data, estimating an erupted lava volume of $6.33 \times 10^6 \pm 3.17 \times 10^6$ m^3 and a mean output rate of 1.26 ± 0.63 m^3/s for the July/August 2019 eruption period. The estimated mean-output-rate was higher than the ones in the 2002–2003 and 2014 Stromboli effusive eruptions, but was lower than in the 2007-eruption. These results confirmed that a multi-sensor-approach might provide a relevant contribution to investigate, monitor and characterize thermal volcanic activity in high-risk areas.

Keywords: Stromboli; infrared satellite imagery; time-averaged discharge rate (TADR); lava flow volume estimation

1. Introduction

Stromboli is part of the Aeolian archipelago, made of six islands and numerous seamounts, which together constitute a Quaternary volcanic arc located in the southern Tyrrhenian basin. It is a stratovolcano showing nearly continuous mild Strombolian activity, alternated with effusive eruptions and/or paroxysmal explosions. An open central conduit that feeds several summit vents aligned NE–SW characterizes the volcano [1–5].

Three different types of explosive activity occur at Stromboli: (*i*) ordinary explosive activity, consisting of low-energy explosions that are repeated every few minutes by the summit; (*ii*) major explosions, similar to the ones that occur during ordinary activity, but they have an energy level about

10 times higher and can produce the fallout of material up to the area called "Il Pizzo sopra la Fossa", overlooking the crater terrace; (*iii*) paroxysmal explosions, of even higher energy, differ from the others due to the involvement of the Stromboli deep feeding system and therefore emit magma which is more fluid magma (or less evolved) and richer in gas. In this last case, an eruption column several kilometers high is formed, with a fallout of coarse material that can reach even the inhabited centers of the island, occasionally forming pyroclastic avalanches and lava flows.

Paroxysmal eruptions are produced by the interaction between a degassed and partially crystallized magma, which stands in the upper part of the central magmatic conduit, and a magma richer in gas, little crystallized, of deep origin. Paroxysm is generated: (*i*) when a greater contribution of deep magma rises quickly breaking into the superficial system [1]; (*ii*) when the deep magma moves to the surface following the emptying of the upper part of the conduit during a prolonged effusive activity [2,3]; (*iii*) when the central conduit collapses and closes generating overpressures, due to the opening of an eruptive vent at low altitude (<500 m above sea level (a.s.l.)) that drains the magma laterally [4–6].

Among the strongest paroxysms documented in the last 100 years, accompanied by the formation of pyroclastic flows and/or tsunamis, there are those of 1906, 1916, 1919, 1930, 1944, 1954, 2003, and 2007 [7,8]. Previously, other eruptions of similar or comparable violence occurred in the sixteenth century.

Major effusive eruptions phases at Stromboli were reported within the last two decades in 2002–2003 [9–11], 2007 [12–14], and 2014 [15]. Minor overflows and short lava fountaining from the summit crater terrace occurred from 2008 until June 2019 (e.g., [6]).

On 3 July 2019, at 14:46 UTC, a rapid sequence of paroxysmal explosions occurred from the summit craters generating an eruption column 4–5 km high. The eruptive column caused the fall of lapilli and incandescent bombs, which burned the vegetation present on the flanks of the volcano. At the same time, two main pyroclastic avalanches, generated by the fall of the erupted material and by the collapse of part of the crater terrace, moved along the Sciara del Fuoco (NW flank of Stromboli) and poured into the sea causing a tsunami wave of about 1 m height.

In the following days, lava overflows occurred from the SW crater area that gave rise to a lava flow that flowing along the Sciara del Fuoco, reached a minimum altitude of about 400 m a.s.l. Incandescent blocks that detached from the front of the lava flows rolled along the slope, accumulating along the coastline. In the following weeks, the explosive activity at the summit craters remained at a high level, despite a progressive reduction in the feeding of the active lava flow along the Sciara del Fuoco being observable.

On 28 August 2019 a second paroxysmal explosion occurred, which generated a single pyroclastic avalanche and a little tsunami. Even after this paroxysm, a lava overflow formed on the Sciara del Fuoco that quickly reached the coastline, but lasted a few hours only. On the evening of 29 August 2019 two major explosions occurred (they were less violent than the previous two paroxysms), in rapid succession, followed by a lava effusion that lasted about a day. From 31 August 2019 onwards, there was a general decrease in eruptive activity.

In this paper, we present the study of the July/August 2019 eruption episode at Stromboli. Thereby, data from different infrared satellites were jointly analyzed.

2. Infrared Satellite-Based Volcano Monitoring

Since the beginning of the Landsat Thematic Mapper (TM) series in 1982, thermal InfraRed (IR) Earth Observation (EO) is an established method for monitoring active volcanoes [16]. IR EO data have been analyzed to study active lava flows (e.g., [17]), lava domes (e.g., [18]), lava lakes (e.g., [19]), and fumarole fields (e.g., [20]). Oppenheimer [21] presented a comprehensive review on volcanic ash and hotspot detection using high temporal resolution data from geostationary sensors as well as higher spatial resolution polar-orbiting sensors, with repeat cycles of at least twice per day such as the Advanced Very High Resolution Radiometer (AVHRR). Over the last three decades, several automated algorithms for volcanic hotspot detection have been developed. Examples are:

(*i*) the contextual VAST [10] and HOTSAT [22] algorithms, which consider the difference between the pixel's temperature and that of its surrounding pixels; (*ii*) MODVOLC [23], performing a single pixel fixed thresholds analysis of Moderate Resolution Imaging Spectroradiometer (MODIS) data, which is used operationally on a global coverage; (*iii*) $\mathrm{RST_{VOLC}}$ detecting volcanic thermal anomalies by the multi-temporal analysis of satellite records [24]; and (*iv*) the Middle InfraRed Observation of Volcanic Activity (MIROVA) system [25], which considers contextual, spectral and temporal properties for hotspot detection.

Hotspot detection algorithms were also developed for processing data from the Advanced Spaceborne Thermal Emission and Reflection Radiometer (ASTER), as shown for example by the ASTER Volcano Archive [26] and by the ASTER Volcanic Thermal Output Database for Latin American Volcanoes [27]. Data from high resolution experimental sensors onboard small satellites, such as the German Aerospace Center (DLR) FireBIRD mission, were analyzed for monitoring the 2014 effusive eruption of Stromboli, Italy [28] and the 2015 eruption of Villarrica Volcano, Chile [29].

Harris et al. [30,31] provided a comprehensive review on the relationship between effusion rates and thermal emission of lava flows.

Focus of our study is the estimation of the time-averaged discharge rate (TADR), which is defined by the lava volume flux averaged over a given time period [32]. Discharge rates are important information for emergency planning and mitigation efforts, as lava flow discharge rates are empirically related to the final area and length of a lava flow (e.g., [33,34]). A direct measurement of the discharge rate provides high precise punctual information, but these instantaneous measurements are only valid for a short time period, due to the high fluctuations of the discharge rate during the activity period of a lava flow [35]. Compared to ground-based measurements, analysis of satellite data enables a faster, less expensive and safer estimation of the TADR (e.g., [20,36]). Satellite techniques show advantages especially during periods when the study area cannot be accessed, as has been the case during the July/August 2019 eruptions at Sciara del Fuoco, Stromboli. Recent examples for infrared satellite-based estimation of the TADR and erupted volume of lava flows are the studies focused on the 2014 effusive eruption episode of Stromboli [28], the 2014–2015 Holuhraun fissure eruption in Iceland [37,38], and the precursors of the 22 December 2018 flank collapse of Anak Krakatau (Indonesia) [39].

3. Materials and Methods

To investigate the eruptive episodes of Stromboli of July/August 2019, we used a multi-sensor satellite approach. First, sensors with high temporal resolution, like SEVIRI (15 min) and AVHRR (~1–6 h), were used to identify eruption onsets and to investigate changes of thermal activity. Then, we used high spatial resolution (HR) satellite data from the Multispectral Instrument (MSI; 10–20 m) and the Operational Land Imager (OLI; 30 m), respectively onboard Sentinel-2 and Landsat-8 satellites, to detect and map lava flow inferring information about the lava effusion period; finally, we performed estimates of TADR and erupted volume using the Visible Infrared Imaging Radiometer Suite (VIIRS) data. VIIRS has on the one hand the advantages to provide data with a high temporal frequency (e.g., it covers the Stromboli island at least twice per day) and at spectral properties which are well suited for TADR estimates, but has on the other hand the disadvantage of providing data with a relatively low spatial resolution (375 m). Consequently, it is not possible to distinguish between thermal activity caused by a lava flow and intense "Strombolian" activity at the central craters using VIIRS data only. Hence, we used the aforementioned HR data for better discrimination of active lava flow from other thermal features. Thereby, the uncertainties due to the low temporal resolution of Sentinel-2 (5 days from the combined constellation [40]) and Landsat-8 (16 days) satellites had to be considered.

3.1. Data

To investigate the Stromboli eruption of July/August 2019 from space, we used data from the following sensors:

(a) SEVIRI, aboard Meteosat Second Generation (MSG) satellites, operates in 12 spectral channels, including the mid-infrared (MIR) band centered at wavelength λ = 3.9 μm, providing data with a spatial resolution of about 3 km at the nadir view. The very high frequency of observation (15 min) makes this instrument suited to identify and characterize short-lived eruptive events and to monitor thermal volcanic activity in real time (e.g., [41]). In this work, we analyzed MSG-SEVIRI data directly acquired and processed at the School of Engineering (SI) of University of Basilicata (Italy).

(b) AVHRR, flying aboard National Oceanic and Atmospheric Administration (NOAA) and Meteorological Operational Satellite (METOP) polar satellites, provides data in five spectral channels, with a spatial resolution of 1 km at the nadir, ranging from visible (VIS) to thermal-infrared (TIR) bands. Channel 3 (λ = 3.55–3.93 μm), which is centered in the MIR region, is the one most suited to identify volcanic thermal anomalies, such as lava flows (e.g., [10]). This channel was used often in combination with the channel 4 (λ = 10.3–11.3 μm) for detecting active magmatic surfaces (e.g., [42–44]). We used here the NOAA/Metop-AVHRR data directly acquired and processed at the Institute of Methodologies for Environmental Analysis (IMAA) of National Research Council (Italy).

(c) MSI and OLI, providing HR data even in the short wave infrared (SWIR) bands at around λ = 1.61 and λ = 2.19 μm, have been efficiently used to study thermal volcanic activity (e.g., [45]) enabling the identification of active vents and the mapping of thermal anomalies (e.g., [46,47]). In this study, we used a series of 16 atmospherically corrected L2A Sentinel-2 MSI datasets [48] for the time-period of 7 June to 26 August 2019 and a single daytime and a nighttime Landsat-8 OLI acquisition, free of clouds over the area of interest (AOI).

(d) VIIRS flying aboard the Suomi National Polar-Orbiting Partnership (Suomi NPP) and the Joint Polar Satellite System (JPSS), has a revisit time over the study area of at least twice per day. To investigate volcanic hotspots at Stromboli volcano, we used the 375 m resolution VIIRS mid IR I4 band (λ = 3.74 μm) and the thermal infrared I5 band (λ = 11.45 μm). In particular, for the time period of 3 July to 30 August 2019 (cf. Section 4) hotspot data from [49], identified over the Sciara del Fuoco, were analyzed [50]. Moreover, the VIIRS product CLDMSK_L2_VIIRS_SNPP was used to consider information on the cloud coverage over the study area during daytime [51].

3.2. Methods

To implement the multi-sensor approach described in the previous section, we used the detailed methods described consecutively:

(a) The Robust Satellite Techniques (RST) multi-temporal approach [52] was applied to infrared SEVIRI data to identify eruption onsets and analyze short-term changes of thermal volcanic activity during the first phase of eruption. In addition, we used the SEVIRI cloud fraction cover (CFC) product, more precisely the fractional cloud cover during night time. This product is derived from the very frequent (every 15 min) geostationary acquisitions and provides daily information about the frequency of cloud coverage of a specific AOI during nighttime [53].

(b) Hotspots identified by the RST_{VOLC} algorithm [24,54], running operationally at IMAA, were investigated to retrieve information on different phases of thermal volcanic activity from infrared nighttime AVHRR records. Only acquisitions with a satellite zenith angle (SZA) < 40° were considered in the analysis.

(c) High spatial resolution multispectral satellite monitoring: For the Sentinel-2 imagery, the band combination 12/11/8A, i.e., SWIR 2 (λ = 2.19 μm), SWIR 1 (λ = 1.61 μm) and Near IR (NIR) (λ = 0.865 μm) was chosen. For the Landsat-8 night time imagery the band combination 7/6 (SWIR 2/SWIR 1) was used. The analysis of the Landsat-8 and Sentinel-2 imagery allowed to detect the beginning of the lava flow and to map its space-time evolution.

(d) Methods for VIIRS IR satellite imagery handling: The VIIRS hotspot product, for which a wide description can be found in [50], was used as input because the full implementation of RST_{VOLC} algorithm on VIIRS data was still in progress at the time of writing. Regarding the used VIIRS hotspot product, it provides the volcanic radiant power (*VRP*) of detected hotspots according to the well-established MIR-approach [55]. Thereby, the *VRP* was derived from the M13 band of VIIRS imagery. The geolocation of VIIRS is more accurate and also its spatial resolution is higher than the one of MODIS and AVHRR (1 km in nadir position), respectively. Therefore, the focus of our lava TADR estimation is based on VIIRS data.

The latter were analyzed here to retrieve the lava *TADR* and erupted lava volume using the approach proposed in [56] (Equations (1) and (2)):

$$TADR = \frac{VRP}{c_{rad}} \tag{1}$$

$$c_{rad} = \frac{6.45 \times 10^{25}}{X_{SiO_2} \times 10^{10.4}} \tag{2}$$

With X_{SiO_2} representing the silica content of the erupted lava in units of weight percent (wt%).

According to Coppola et al. [56], when estimating c_{rad}, one has to take into account the strong effects that the bulk rheology has on the spreading and cooling processes of active lava. Therefore, an uncertainty of ±50% c_{rad} has to be considered. Consequently, a maximum and a minimum *TADR* calculation were performed with $c_{rad,min} = c_{rad} \cdot 0.5$ and $c_{rad,max} = c_{rad} \cdot 1.5$, respectively. The following steps were performed for the minimum and the maximum *TADR* estimates, and for the mean of both.

Next, the *TADR* values of each single hotspot detected within one satellite acquisition were summed up to $TADR_t$. The erupted lava volume V_t was retrieved by calculating the integral of the *TADR* of two sequential satellite acquisitions t_i and t_j (Equation (3)). The entire erupted lava volume *V* was derived by cumulatively summing up V_t (Equation (4)).

$$V_t = \int_{t_i}^{t_j} TADR_t(t)dt = \left(t_j - t_i\right)\frac{TADR_{t_j} + TADR_{t_i}}{2} \tag{3}$$

$$V = \sum V_t \tag{4}$$

Typical values for X_{SiO_2} for low-porphyritic (LP) volatile-rich magma, which erupted during July/August 2019, are 49.12 wt% to 49.19 wt% [57]. For a first *TADR* and lava volume estimation, the mean value of the above-mentioned endmembers was used: X_{SiO_2} = 49.155 wt%. The effects of the variation of X_{SiO_2} are discussed in Section 5.

In addition to the rheological variation of the lava, also external effects influence the TADR and lava volume estimation: (*i*) the reliability of hotspots detection due to scan angle effects and (*ii*) cloud coverage of the AOI. The following steps were performed to mitigate these uncertainties (Table 1):

As the satellite scan angle strongly influences the reliability of volcanic hotspot detection, we additionally calculated the TADR by only considering hotspots that were acquired at a scan angle from nadir to ≤31.59° (cf. Table 1, Scenario II). We used this scan angle region, because it corresponds to the first aggregation region of VIIRS, where three native pixels are aggregated along scan direction to form one data sample in the Level 1 image [50]. Our scan angle threshold corresponds well with the findings of [25], who suggested excluding imagery with satellite scan angles > 30°, since at such high viewing angles hotspots located in deep craters or at steep slopes may not be detected. Moreover, high scan angles deform the projected thermal anomaly and reduce the geolocation accuracy of the hotspots.

Cloud coverage of the AOI prevents the detection of volcanic hotspots. Partly cloud coverage of the AOI leads to a reduced number of detected hotspots, i.e., the *VRP* emitted by the erupted lava and therefore the TADR and lava volume are underestimated. To reduce this effect of a partly cloudy AOI, at least for daytime acquisitions, we performed an additional TADR estimation by considering, in addition to all nighttime hotspots, only such daytime hotspots which were acquired at clear sky conditions. A previous independent paper [38] also described the exclusion of acquisitions, which are affected by clouds over the AOI. The information of cloud coverage during the daytime VIIRS overflights was derived from the product CLDMSK_L2_VIIRS_SNPP (cf. Table 1, Scenario III).

Cloud detection during nighttime is more complicated than during daytime. Since for VIIRS there is no nighttime cloud product available, we analyzed the SEVIRI cloud fraction cover (CFC) product, (see (a) in Section 3.2). To ensure that the TADR estimation is not affected by partly cloud coverage of the AOI, only those VIIRS acquisition dates which showed a cloud cover fraction of 0% in the SEVIRI CFC nighttime product were considered. We therefore calculated an additional scenario, which in addition to the clear sky daytime acquisitions (based on the VIIRS cloud mask) also considered cloud-free nighttime acquisitions (cf. Table 1, Scenario IV).

As during nighttime no information about possible (partly) cloud coverage of the AOI could directly be derived from the VIIRS data, an additional TADR estimation based on only hotspots acquired at clear sky daytime acquisitions was performed (cf. Table 1, Scenario V).

In conclusion, we estimated the TADR and erupted lava volume for five scenarios with each one considering the aforementioned variation of c_{rad} (Table 1).

Table 1. Scenarios for Visible-Infrared-Imaging-Radiometer-Suite (VIIRS) data-based time-averaged discharge rate (TADR) and lava volume estimation.

Scenario	Description
I	Considering the *VRP* measurements from all hotspots detected over the AOI
II	Considering only *VRP* measurements with scan angles ≤ 31.59°
III	In addition to scenario II: considering only clear sky acquisitions (for the daytime acquisitions) and in addition all nighttime acquisitions
IV	In addition to scenario III: considering in addition to the clear sky daytime acquisitions only clear sky nighttime acquisitions (SEVIRI nighttime CFC = 0%)
V	Same as scenario III, but considering only the daytime acquisitions with clear sky

4. Results

Figure 1 displays the temporal trend of the SEVIRI brightness temperature measured in the MIR channel $BT_{MIR}(x,y)$ (blue curve, with a 15 min temporal sampling), retrieved over the pixel (x,y), including the Stromboli crater area, in reference to the period 1–8 July 2019.

The plot also displays the curve of temporal mean $\mu_{MIR}(x,y)$ and of $\mu_{MIR}(x,y) \pm 3\sigma_{MIR}(x,y)$ (where $\sigma_{MIR}(x,y)$ is the temporal standard deviation), derived for the aforementioned pixel according to the RST guidelines [52].

Figure 1 shows that $BT_{MIR}(x,y)$ was in the range $\mu_{MIR}(x,y) \pm 3\sigma_{MIR}(x,y)$ until the morning of 3 July 2019, when we recorded a first anomalous increase in the MIR signal (i.e., $BT_{MIR}(x,y) > \mu_{MIR}(x,y) + 3\sigma_{MIR}(x,y)$) at 08:15 UTC and 08:45 UTC, possibly marking the intensification of Strombolian activity at the craters. A few hours later, i.e., 14:45 UTC, a more abrupt increase of $BT_{MIR}(x,y)$ occurred, marking the start of the powerful explosion at Stromboli, in perfect agreement with field observations. In the following hours, the analyzed signal (see blue curve) remained at very high values (with a peak observed on 4 July, at 04:15 UTC with a maximum intensity up to ~$37\sigma_{MIR}(x,y)$) due to the ongoing eruption. Nonetheless, other sudden anomalous variations of $BT_{MIR}(x,y)$ were recorded in the following days, as indicated by changes in the signal slope marking short-term increments in the intensity of volcanic thermal emissions (e.g., 4 July at 04:15 UTC; 6 July 08:30 UTC). These changes of thermal activity were presumably associated with lava spattering, a small lava flow, and intermittent Strombolian activities occurring at the monitored volcano (e.g., [58]).

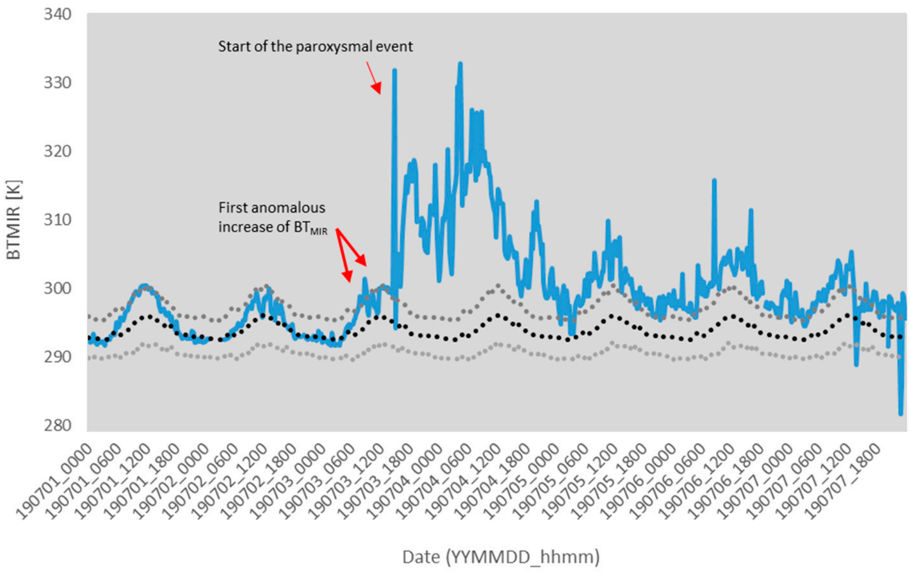

Figure 1. Temporal trend of Spinning-Enhanced-Visible-and-InfraRed-Imager (SEVIRI) mid-infrared (MIR) channel data $BT_{MIR}(x,y)$ (blue curve) recorded during the period 1–8 July 2019 over Stromboli. In black, the curve of $\mu_{MIR}(x,y)$; in light and dark grey the curve of $\mu_{MIR}(x,y) \pm 3\sigma_{MIR}(x,y)$. SEVIRI MIR channel data of 3 July at 08:45 UTC with indication of pixel ($BT_{MIR}(x,y)$ = 309.65 K) appearing anomalous before the start of the paroxysm.

Figure 2 displays the temporal trend of hotspot pixels detected in AVHRR imagery during July/August 2019. It is worth noting that RST_{VOLC} flagged a thermal anomaly since 2 July 2019 in agreement with field observations (see also Sentinel-2 MSI data of the same day shown in (Figure 3e). The day after (i.e., 3 July), the number of hotspot pixels significantly increased because of paroxysm. On 4 July 2019, RST_{VOLC} revealed a further increase of thermal activity, fitting with the information retrieved from SEVIRI data. Afterwards, the hotspot pixel number fluctuated also because of clouds, which partially/completely masked the AOI, revealing however some minor increments in volcanic thermal emissions in other days of July and August (e.g., 27 July and 20 August 2019).

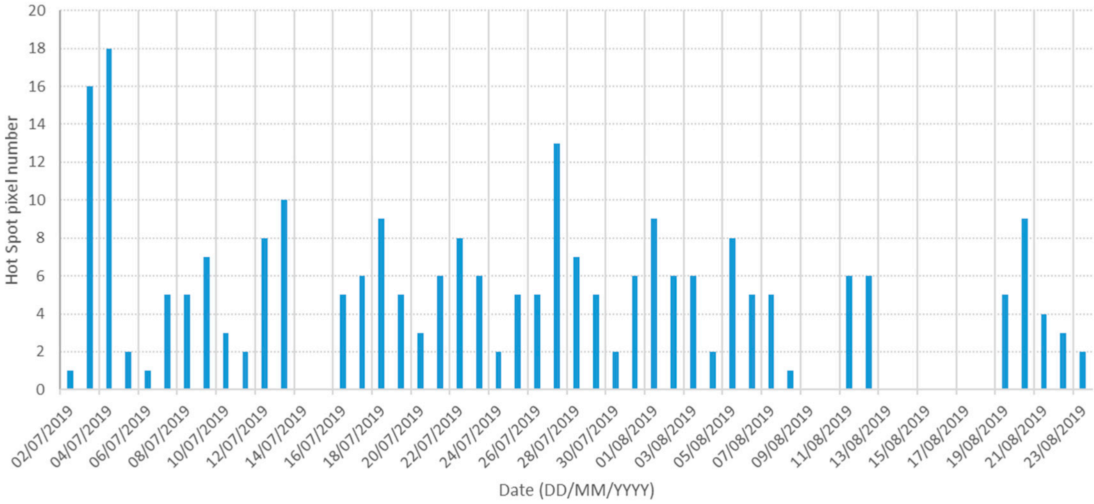

Figure 2. Thermal anomalies detected by the RST_{VOLC} algorithm over Stromboli volcano processing nighttime Advanced-Very High-Resolution-Radiometer (AVHRR) data during June/August 2019. Note that fluctuations in the hotspot pixel number were also due to cloud effects.

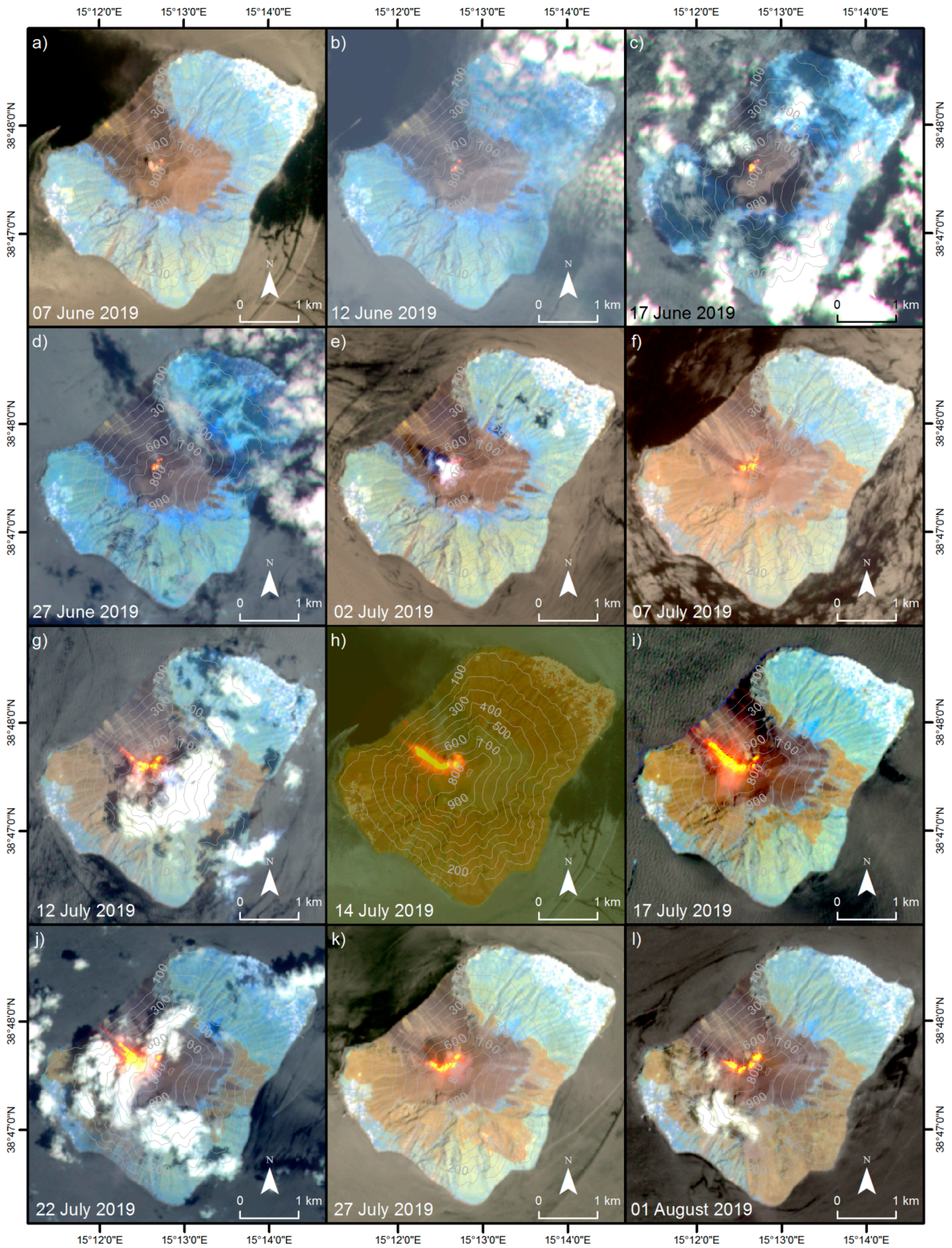

Figure 3. False color imagery of Stromboli acquired by (**a**–**g**,**i**–**l**) Sentinel-2 with band combination 12/11/8A and (**h**) by Landsat-8 at night time with band combination 7/6 overlaid on the Sentinel-2 acquisition from 7 June 2019. Thermal activity at the central craters can be seen at all acquisitions. Active lava flows moving down the Sciara del Fuoco (NW slope of Stromboli) are visible from 7 July to 1 August 2019. Contour lines derived from ALOS DEM.

To map the lava flows at the Sciara del Fuoco in a more accurate way, better discriminating the effusion period, we analyzed a time series of false color imagery, at high spatial resolution, acquired from 7 June to 26 August 2019, as shown in Figures 3 and 4. Except for two images (Figures 3h and 4b), they were acquired by Sentinel-2 and show the sea around the Stromboli Island in grey color, built up areas (e.g., the Stromboli and Ginostra towns) in white color, areas of living vegetation in blue, and areas free of vegetation in brown colors. Thermal activity, e.g., due to lava flow, is shown in yellow and orange colors, using the band combination 12/11/8A.

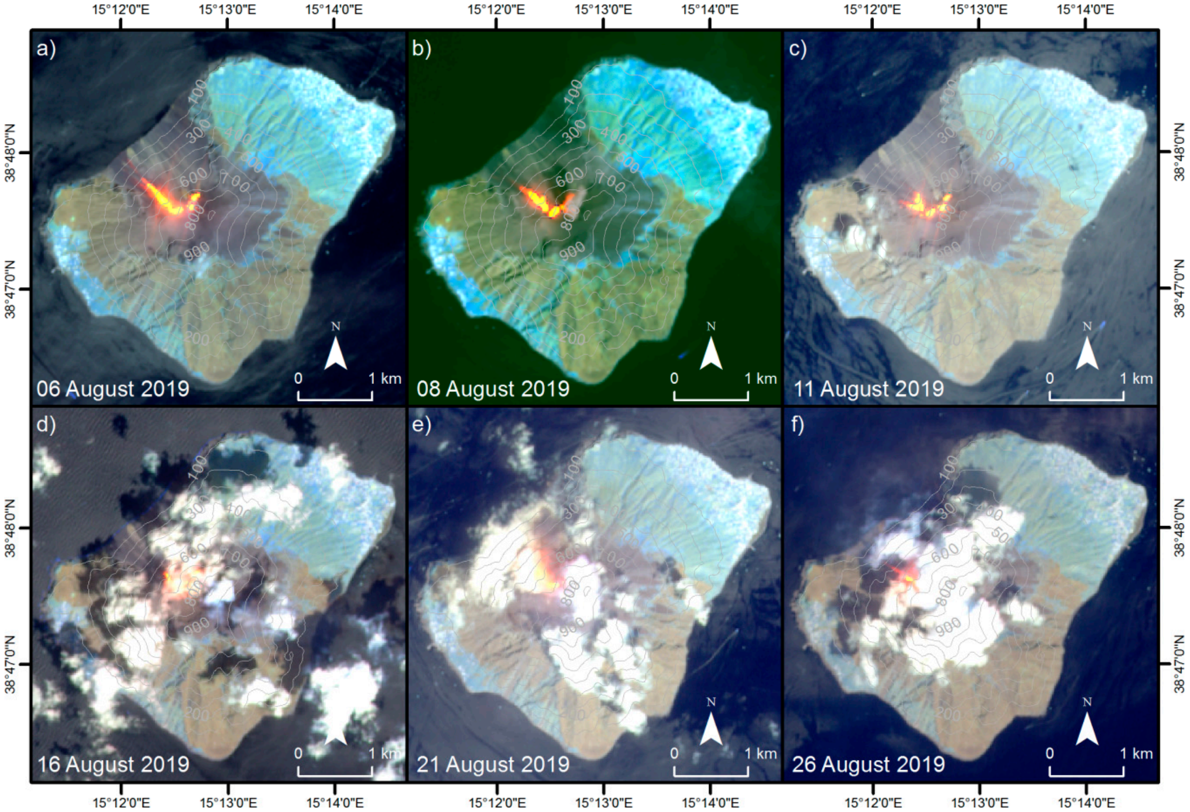

Figure 4. False color imagery of Stromboli acquired by (**a**,**c**–**f**) Sentinel-2 with band combination 12/11/8A and (**b**) by Landsat-8 with band combination 7/6/5. The first three images (**a**–**c**) show lava flows at clear sky conditions. Although the other three acquisitions (**d**–**f**) are partly cloudy, thermal activity due to active lava flows moving down the Sciara del Fuoco (NW slope of Stromboli) can be seen. Contour lines derived from ALOS DEM.

From 7 June–2 July 2019, there was a continuous thermal activity visible at the Stromboli central craters, but no strong change occurred during this time.

Between 2 July and 7 July 2019 (Figure 3e,f), a strong change affected the Stromboli Island: The formerly vegetation covered SE and SW slopes were now covered by ash/tephra and the area free of vegetation on the NW slope (Sciara del Fuoco) extended towards NE and SW direction. We assumed that the loss of vegetated area was due to the large eruption event on 3 July 2019 (cf. Section 1).

Relatively large lava flows, which flowed down to ca. 480 m, 300 m, and 200 m a.s.l., were evident on satellite scenes of 12, 14 and 17 July 2019 (Figure 3g–i), respectively. On 22 July 2019 lava flowed down to ca. 325 m a.s.l. (Figure 3j), while on 27 July and on 1 August 2019 active lava flows down to 500 m a.s.l. were observed (Figure 3k,l). Figure 4a–c shows active lava flows down to ca. 300 m, 390 m, and 500 m a.s.l., respectively. The scenes shown in Figure 4d–f are partly affected by clouds, which makes an exact location of active lava flows difficult. Nevertheless, we estimated that the lava flowed down to around 580 m and 400 m a.s.l., respectively, from these images.

The analysis of Sentinel-2 MSI and Landsat-8 OLI then revealed the presence of a lava effusion at the Sciara del Fuoco since 7 July continuing in August; i.e., when $\mathrm{RST_{VOLC}}$ still flagged the presence of a thermal anomaly at the target area (see Figure 2).

To characterize the lava effusion at the Sciara del Fuoco from a quantitative point of view, we estimated both TADR and lava volume using the hotspots derived from 108 VIIRS scenes, which were acquired from 3 July to 30 August 2019. The first hotspot was detected on 4 July 2019. Table 2 and Figures 5–14 show the results of these estimations for the five scenarios of the VIIRS data based on analysis described in Table 1. The deviation of the TADR, cumulative lava volume, and the mean lava output rate within each scenario are due to the ±50% uncertainty, which has to be considered for the c_{rad}. Using $X_{SiO_2} = 49.155$ wt% in Equation (2) results in a c_{rad} ranging from $8.25 \times 10^7 \frac{\mathrm{J}}{\mathrm{m}^3}$ to $2.47 \times 10^8 \frac{\mathrm{J}}{\mathrm{m}^3}$.

Table 2. VIIRS data-based TADR and lava volume estimation for the five scenarios described in Table 1.

Scenario	Number of Useful VIIRS Acquisitions	Number of Valid Hotspots	Maximum TADR Measurement [m^3/s]	Day and Time [UTC] of Max. TADR Measurement	Cumulative Lava Volume [m^3]	Mean Lava Output Rate [m^3/s] Over 58 Days
I	108	593	8.03 ± 4.02	22 July 2019 at 01:36	$5.76 \times 10^6 \pm 2.88 \times 10^6$	1.15 ± 0.57
II	88	481	8.03 ± 4.02	22 July 2019 at 01:36	$5.70 \times 10^6 \pm 2.85 \times 10^6$	1.14 ± 0.57
III	81	467	8.03 ± 4.02	22 July 2019 at 01:36	$5.85 \times 10^6 \pm 2.93 \times 10^6$	1.17 ± 0.58
IV	33	165	8.03 ± 4.02	22 July 2019 at 01:36	$6.33 \times 10^6 \pm 3.17 \times 10^6$	1.26 ± 0.63
V	17	45	4.72 ± 2.36	22 July 2019 at 11:18	$6.41 \times 10^6 \pm 3.20 \times 10^6$	1.28 ± 0.64

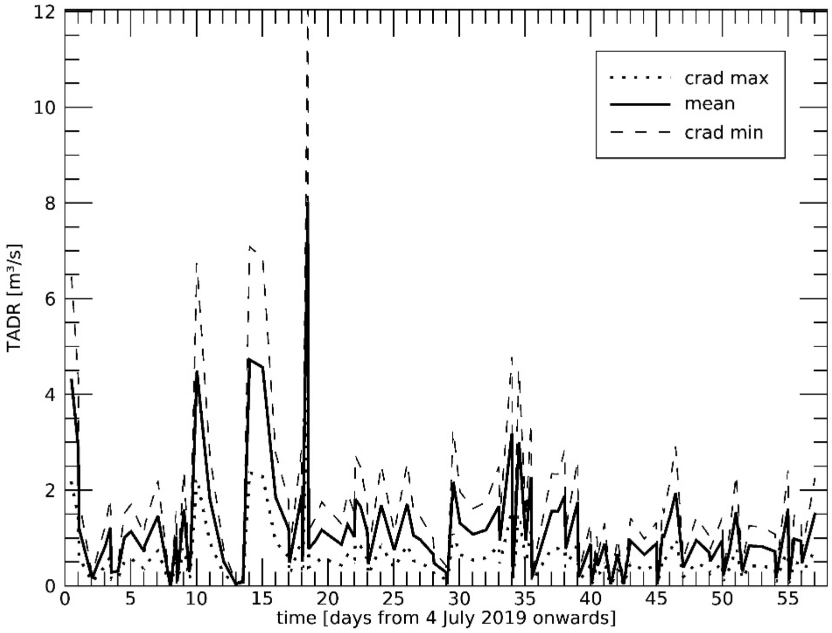

Figure 5. VIIRS data-based temporal evolution of the estimated TADR (m^3/s) from 4 July to 30 August 2019. All VIIRS hotspots that were within the aforementioned time period detected over the central craters and the Sciara del Fuoco were considered (scenario I). The dotted line shows the results for $c_{rad} = 2.47 \times 10^8 \frac{\mathrm{J}}{\mathrm{m}^3}$, the dashed line the results for $c_{rad} = 8.25 \times 10^7 \frac{\mathrm{J}}{\mathrm{m}^3}$, which are the corresponding values of $X_{SiO_2} = 49.155$ wt%. The solid line represents the mean of the TADR estimation.

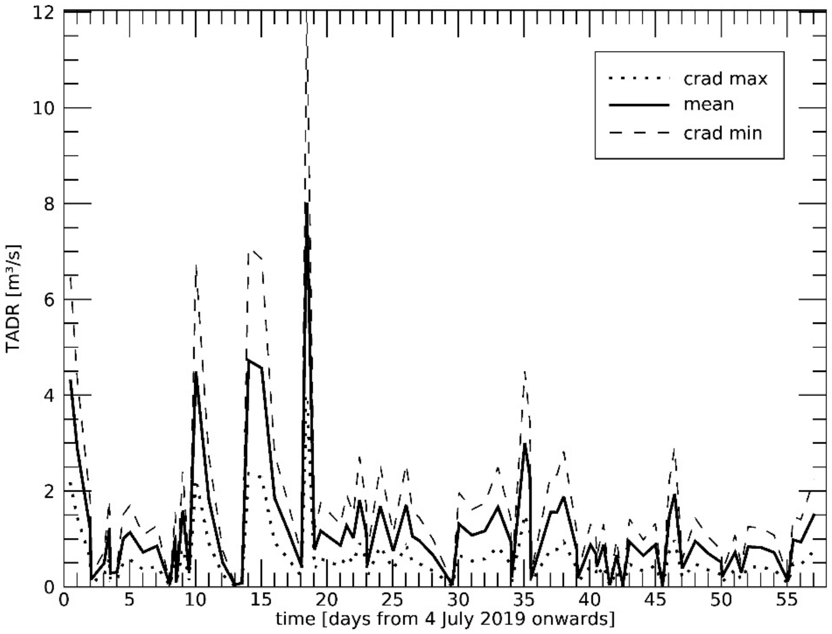

Figure 6. Same as Figure 5, however, only VIIRS hotspots acquired at a scan angle ≤ 31.59° off-nadir were considered (scenario II).

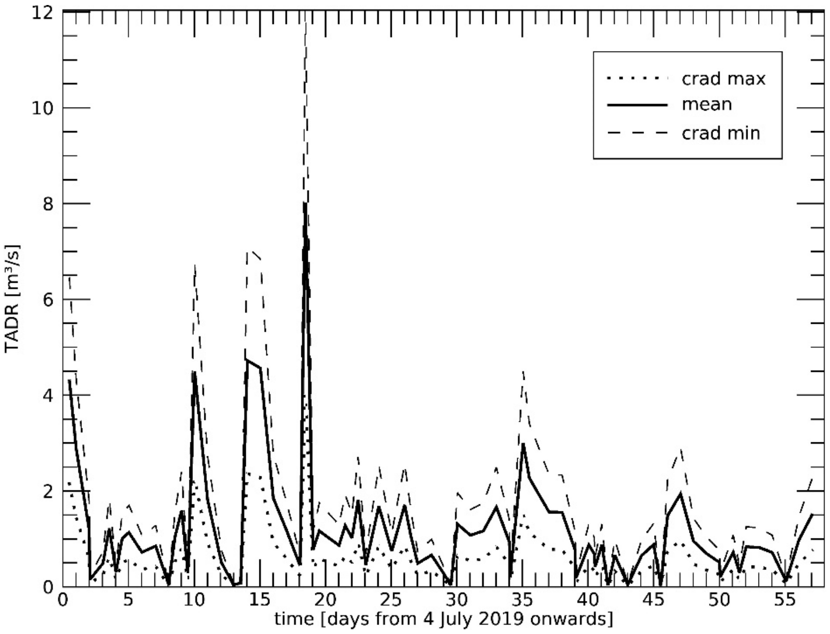

Figure 7. Same as Figure 6, however, for the daytime acquisitions only those with clear sky conditions were considered. Moreover, all nighttime acquisitions were taken into account (scenario III).

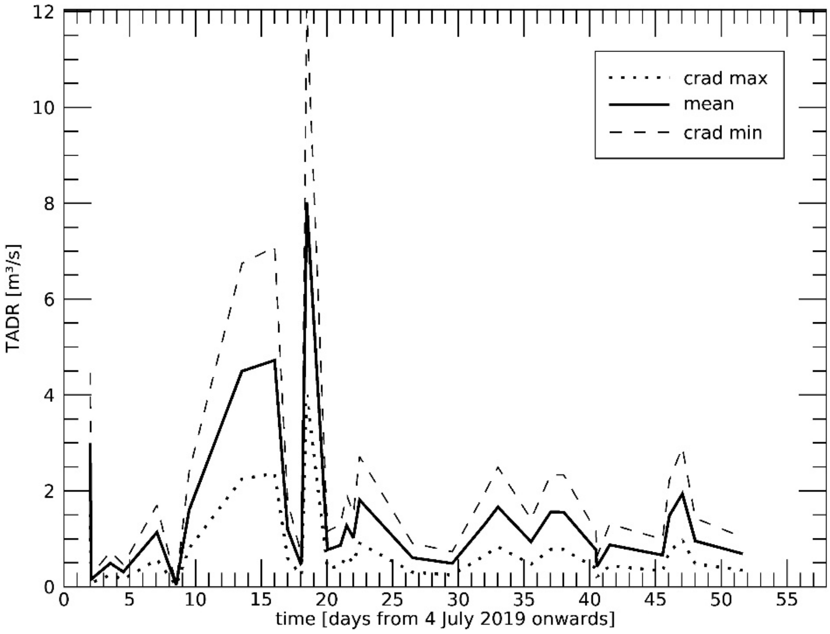

Figure 8. Same as Figure 7, however, in addition, also for the nighttime acquisitions only those with clear sky conditions were considered (scenario IV).

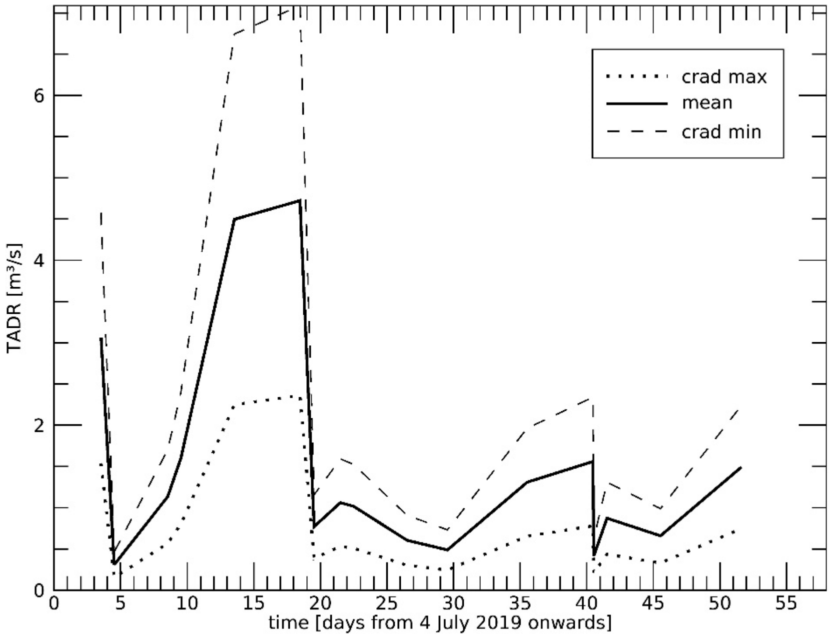

Figure 9. Same as Figure 7, however, only the clear sky daytime acquisitions were considered (no nighttime acquisitions) (scenario V).

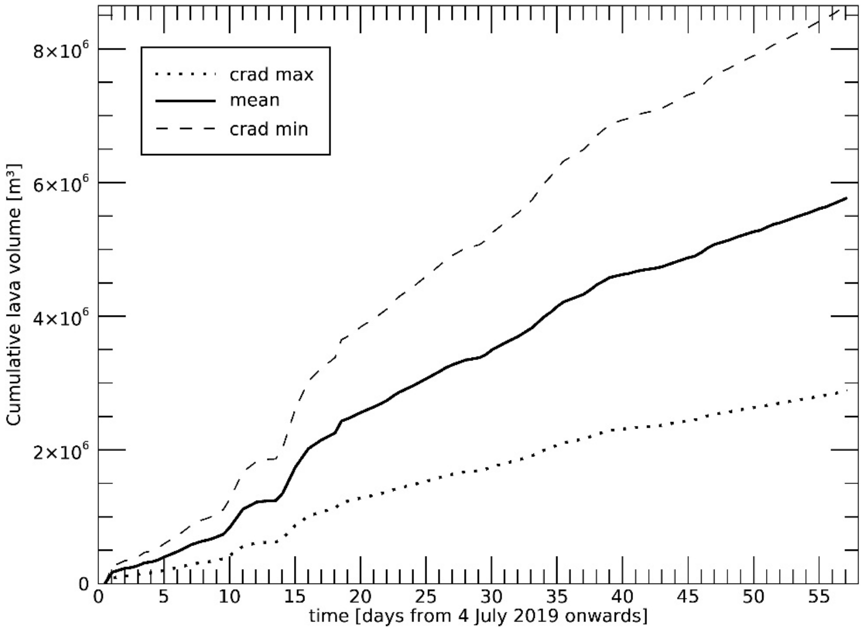

Figure 10. VIIRS data-based temporal evolution of the cumulative volume (m^3) of erupted lava based on the TADR estimation shown in Figure 5 (scenario I).

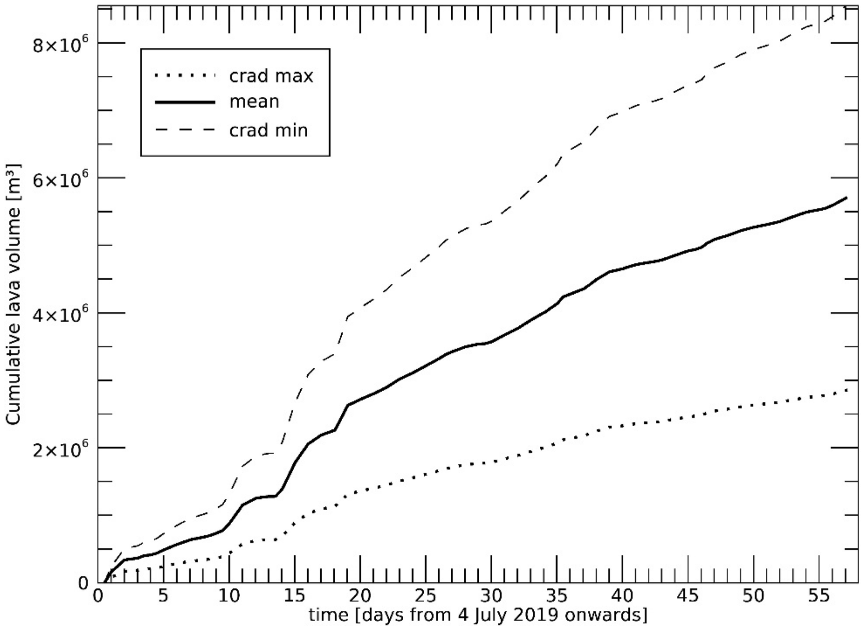

Figure 11. VIIRS data-based temporal evolution of the cumulative volume (m^3) of erupted lava based on the TADR estimation shown in Figure 6 (scenario II).

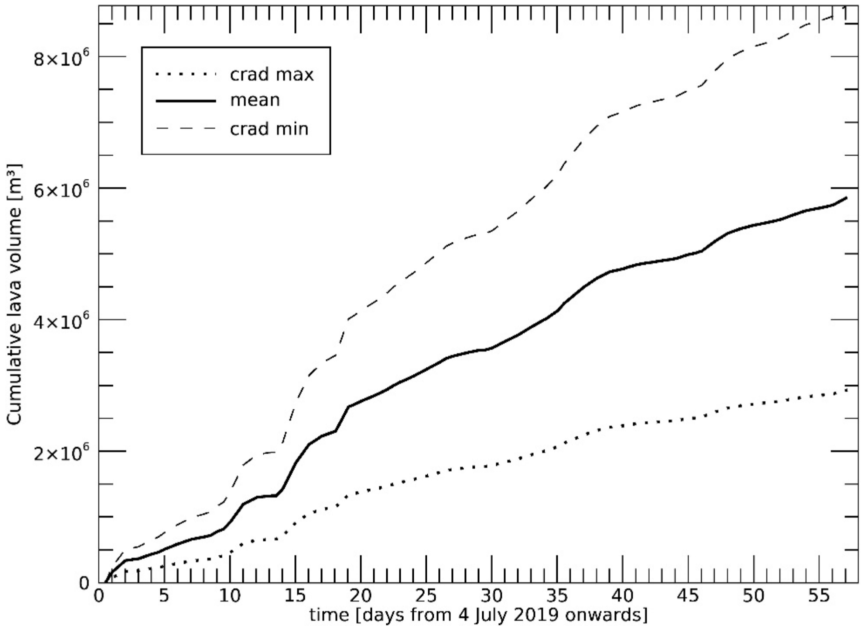

Figure 12. VIIRS data-based temporal evolution of the cumulative volume (m^3) of erupted lava based on the TADR estimation shown in Figure 7 (scenario III).

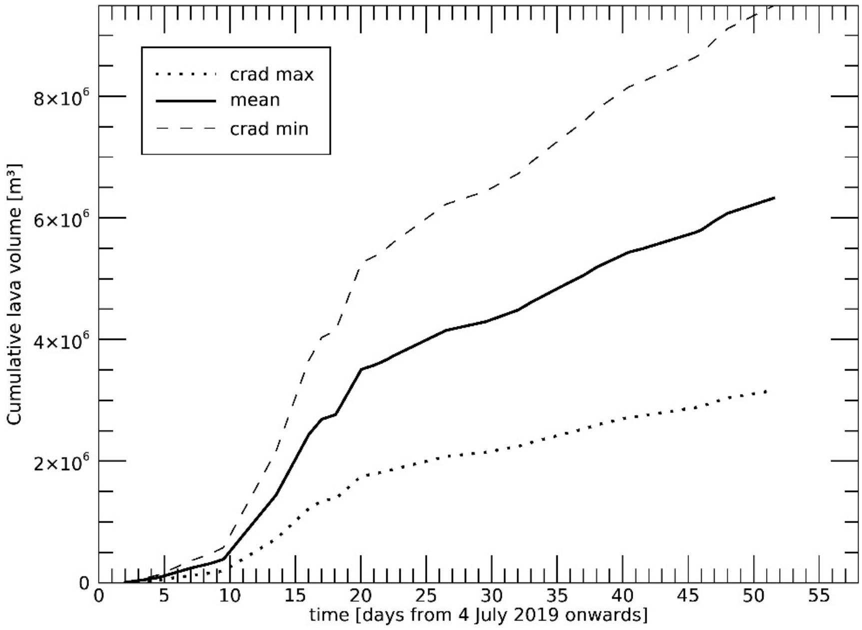

Figure 13. VIIRS data-based temporal evolution of the cumulative volume (m^3) of erupted lava based on the TADR estimation shown in Figure 8 (scenario IV).

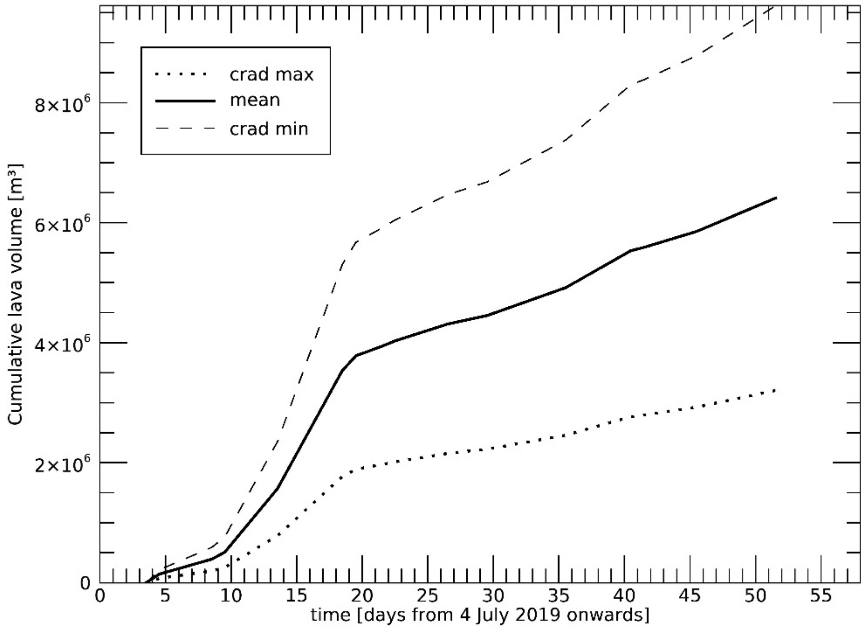

Figure 14. VIIRS data-based temporal evolution of the cumulative volume (m^3) of erupted lava based on the TADR estimation shown in Figure 9 (scenario V).

The highest TADR value of 8.03 ± 4.02 m^3/s was measured in the VIIRS acquisition on 22 July 2019 at 01:36 UTC (for the first four scenarios). As scenario V) considers only daytime acquisitions, the highest TADR value estimated for this scenario is 4.72 ± 2.36 m^3/s, measured on 22 July 2019 at 11:18 UTC.

Table 2 shows that 20 VIIRS acquisitions (corresponding to 112 hotspots) were excluded in scenario II compared to scenario I), as these were acquired at too large scan angles. This results in a slight decrease of the estimated cumulative lava volume of ca. 60,000 m^3. The additional exclusion of nine VIIRS acquisitions (corresponding to 14 hotspots), due to partly cloud coverage of the AOI during daytime, results in an increase of ca. 150,000 m^3 of estimated lava volume (in comparison to scenario II. The mean lava output rates of the first three scenarios are very similar.

In scenario IV another 48 VIIRS scenes (corresponding to 302 hotspots) were excluded due to possible cloud coverage during nighttime (based on the SEVIRI cloud cover fraction nighttime product, cf. (see (a) in Section 3.2). This increases the estimated lava volume by ca. 480,000 m^3.

Only 16% of the VIIRS scenes acquired over the AOI during the observation period and only 8% of the original detected VIIRS hotspots fulfill the requirements of scenario V, i.e., were acquired at daytime, clear sky, and low scan angles. Using only these 45 hotspots results in an increase of ca. 80,000 m^3 of the cumulative lava volume (in comparison to scenario IV). The mean lava output rates of the scenarios IV and V are comparable.

5. Discussion

By analyzing infrared SEVIRI data by means of RST_{VOLC} approach, we retrieved information about the start of the paroxysmal event at Stromboli Volcano. Moreover, the same analysis revealed changes of thermal volcanic activity in the days immediately after the start of the paroxysm, in agreement with information provided by nighttime AVHRR observations. To assess these changes of thermal activity, we investigated the Sentinel-2 MSI and Landsat-8 OLI scenes available during the period of interest. High spatial resolution satellite imagery revealed the presence of a lava flow at the Sciara del Fuoco since 7 July; i.e., four days after the start of the paroxysms. On the other hand, according to Istituto Nazionale di Geofisica e Vulcanologia (INGV), the lava effusion took place at Stromboli volcano during 3 July–30 August 2019 [58]. Hence, if on the one side Sentinel-2 MSI and

Landsat-8 OLI imagery enabled an accurate localization of volcanic thermal anomaly on the other side they did not allow us to assess the presence of an active lava flow during 3–6 July (i.e., when SEVIRI/AVHRR observations revealed changes in thermal volcanic activity), due to the low temporal sampling. These analyses confirmed the importance of combining different satellite observations for better investigation of active volcanic areas.

In reference to the quantitative characterization of the active lava flows, in Table 2 and Figures 5–14 we have shown the variations of the estimated erupted lava volume, and the mean lava output rate, in relationship to the five scenarios described in Table 1. Exclusion of VIIRS scenes where the AOI was acquired at too large scan angles is a reasonable approach as described see (d) in Section 3.2. The threshold for the scan angles was set equal to the first pixel aggregation level of VIIRS data, which is also close to the value suggested by [25]. The influence of this step on the estimated lava volume is very low with a decrease of 1.0% compared to scenario I.

Exclusion of hotspots detected in partly cloudy acquisitions over the AOI is an important step [38]. Scenario III considers only the information on cloud coverage during daytime and shows a 2.6% increase of the estimated lava volume compared to scenario II. Scenario IV considers in addition also information about possible cloud coverage of the AOI during nighttime. Scenario IV shows an 8.2% increase of the estimated lava volume compared to scenario III and 11.1% increase compared to scenario II.

The VIIRS cloud mask is more accurate due to (*i*) its higher spatial resolution compared to that of the SEVIRI data and (*ii*) the VIIRS cloud mask provides information about (partial) cloud coverage of the AOI exactly at the time when the hotspots were detected, while the SEVIRI data only provides information about the fraction of cloud coverage over the AOI during an entire night. However, only 17 VIIRS acquisitions, which represent 8% of all analyzed VIIRS acquisitions (or 16% of the detected hotspots), were detected at clear sky and low scan angles during daytime (scenario V). A TADR and lava volume estimation based only on this low number of observations during the 2-months investigation period would be not meaningful. 33% of the VIIRS acquisitions acquired over the AOI during the observation period fulfill the requirements of scenario IV: Clear sky day and night and low scan angles. Consequently, we consider the results of scenario IV the most meaningful one: $6.33 \times 10^6 \pm 3.17 \times 10^6$ m^3, which results in a mean lava output rate of 1.26 ± 0.63 m^3/s. Nevertheless, both scenarios IV and V show very similar results, with only a slight increase of the estimated lava volume of 1.3% compared to scenario IV. As described in Section 3.2, LP magma, which erupted during July/August 2019, is characterized by silica contents ranging from X_{SiO_2} min = 49.12 wt% to X_{SiO_2} max = 49.19 wt%. Therefore, in addition to the TADR and lava volume estimation based on X_{SiO_2} = 49.155 wt% described above, these parameters were also calculated based on X_{SiO_2} min = 49.12 wt% to X_{SiO_2} max = 49.19 wt%. Thereby, the most meaningful scenario, scenario IV, was applied (Figures 15–18).

Table 3 shows the corresponding estimated erupted lava volumes for the different silica contents.

Table 3. VIIRS data-based lava volume estimation for different silica contents, based on scenario IV.

Silica Content X_{SiO_2} [wt%]	**c_{rad} min $[\frac{J}{m^3}]$**	**c_{rad} max $\left[\frac{J}{m^3}\right]$**	**Cumulative Lava Volume [m^3]**	**Mean Lava Output Rate [m^3/s] Over 58 Days**
49.12	8.3×10^7	2.49×10^8	$6.28 \times 10^6 \pm 3.14 \times 10^6$	1.25 ± 0.63
49.155	8.25×10^7	2.47×10^8	$6.33 \times 10^6 \pm 3.17 \times 10^6$	1.26 ± 0.63
49.19	8.18×10^7	2.46×10^8	$6.37 \times 10^6 \pm 3.18 \times 10^6$	1.27 ± 0.64

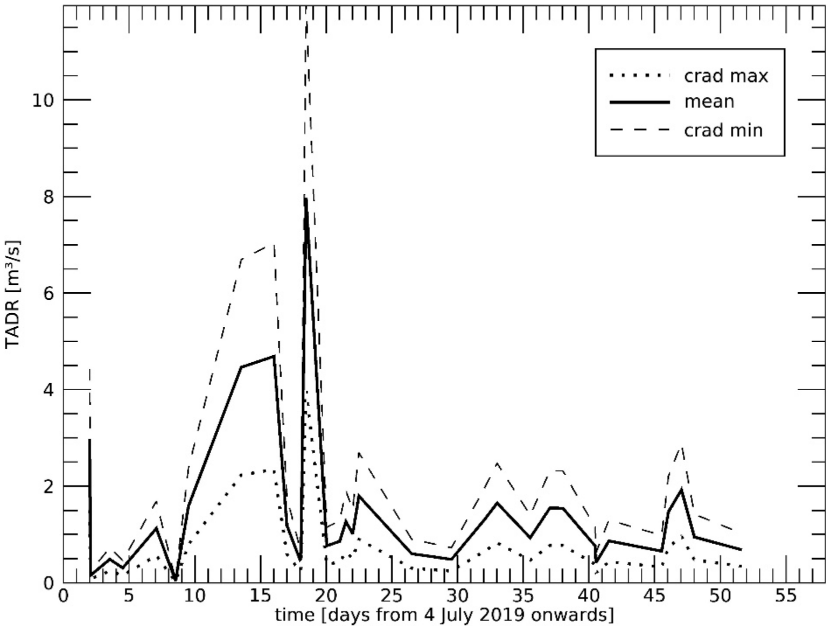

Figure 15. VIIRS data-based temporal evolution of the estimated TADR (m^3/s) from 4 July to 30 August 2019, applying scenario IV with X_{SiO_2} = 49.12 wt%. The dotted line shows the results for $c_{rad} = 2.49 \times 10^8 \, \frac{\mathrm{J}}{\mathrm{m}^3}$, the dashed line the results for $c_{rad} = 8.31 \times 10^7 \, \frac{\mathrm{J}}{\mathrm{m}^3}$. The corresponding value of the solid line represents the mean of the TADR estimation.

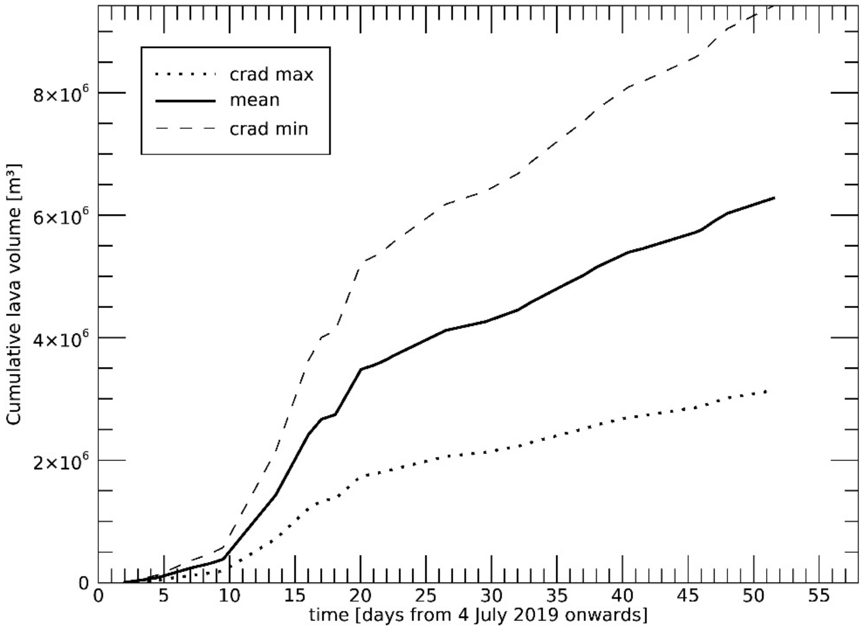

Figure 16. VIIRS data-based temporal evolution of the cumulative volume (m^3) of erupted lava based on the TADR estimation shown in Figure 15 (scenario IV) with X_{SiO_2} = 49.12 wt%.

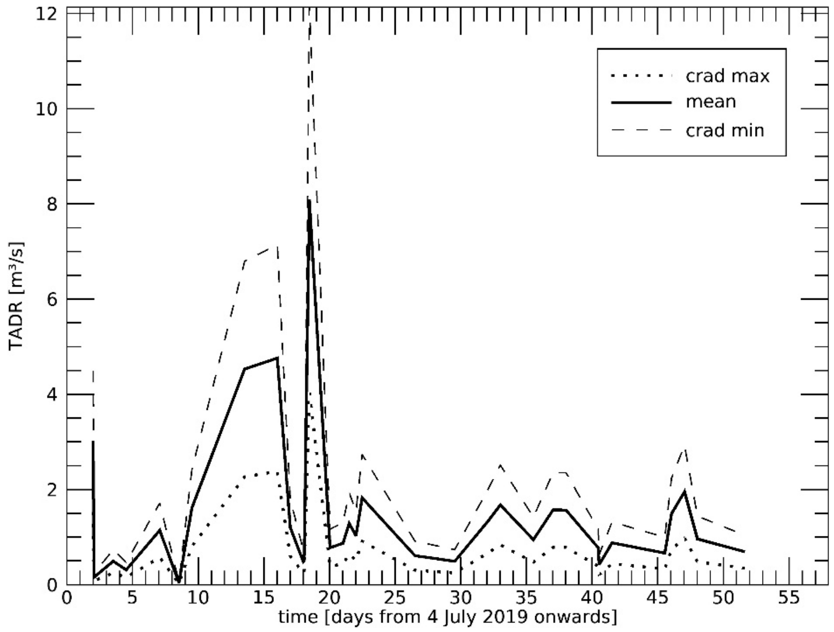

Figure 17. VIIRS data-based temporal evolution of the estimated TADR (m^3/s) from 4 July to 30 August 2019, applying scenario (IV) with X_{SiO_2} = 49.19 wt%. The dotted line shows the results for $c_{rad} = 2.46 \times 10^8 \ \frac{\text{J}}{\text{m}^3}$, the dashed line the results for $c_{rad} = 8.18 \times 10^7 \ \frac{\text{J}}{\text{m}^3}$. The corresponding value of the solid line represents the mean of the TADR estimation.

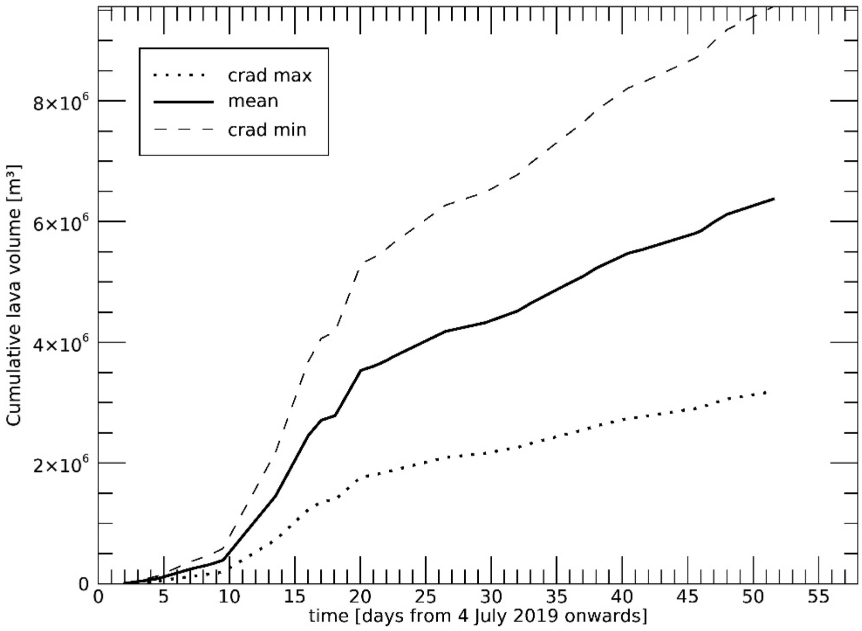

Figure 18. VIIRS data-based temporal evolution of the cumulative volume (m^3) of erupted lava based on the TADR estimation shown in Figure 17 (scenario IV) with X_{SiO_2} = 49.19 wt%.

When taking the variation of X_{SiO_2} from 49.12–49.19 wt% into account, the estimates for the mean lava output rate range from 1.25 ± 0.63 m^3/s to 1.27 ± 0.64 m^3/s, that we observed for the July/August 2019 lava flow events. This mean output rate is higher than the mean output rates reported for the 2002–2003 (0.32 ± 0.28 m^3/s) [11] and the 2014 effusive eruptions (ca. 0.87 m^3/s [29]), but is lower than the mean output rate reported for the 2007 event (ca. 2.4 m^3/s [12]).

It is worth mentioning that, from a structural point of view, the July/August 2019 eruption was very different from those occurring in 2002–2003 and in 2007. In the previous cases, eruptions were mainly effusive from lateral vents, placed at lower altitudes (400–700 m a.s.l.), while intense explosive activities were rare and short (minutes to hours), at the beginning of the eruptive phases or during the course of the eruptions. Therefore, in 2002–2003 and in 2007, eruptions were characterized by a continuous lateral drainage of the magma spilled out from lateral vents, while the Strombolian activity of the summit disappeared [4,5].

Instead, in July/August 2019 the scenario was completely different. The structural framework of the volcano remained stable, and no lateral vents were opened. The eruption was concentrated entirely within the summit crater terrace (>750 m a.s.l.), while the lava overflowed more or less abundantly from the terrace along the Sciara del Fuoco only during the increase of the effusion rate. We can therefore describe this eruption as a long period (about two months) of very intense Strombolian explosive activities, some paroxysmal, accompanied by (*i*) formation of lava flows inside the summit crater terrace; (*ii*) nearly continuous overflows on the Sciara del Fuoco; and (*iii*) fallout of incandescent material coming from explosions, rolling down to the sea coast.

From 2007 onwards, the eruptive activity of Stromboli was characterized by an increase in explosive activities, both in frequency and energy, accompanied almost exclusively by overflows from the summit crater terrace [6]. The July/August 2019 eruption fits exactly into this trend, but it was characterized by explosive intensities/frequencies never reached in recent decades. This evolution could be determined by a modification of the shape of the uppermost central conduit, which has become progressively wider and warmer due to the movements that occurred in the Sciara del Fuoco after the 2002 landslide events, and due to the graben-like collapses of the summit craters that occurred in 2007 [4–6,59]. Therefore, the present geometric configuration of the shallow portion of the feeder conduit seems to decrease the probability of lateral dike intrusions and to favor an increase of activity at summit craters [6].

6. Conclusions

Following the rapid sequence of paroxysmal explosions at the summit craters of Stromboli on 3 July 2019, an episode of higher eruption activity occurred during the rest of July until the end of August 2019. In this study, we have analyzed this recent eruption episode by using a multi-sensor data approach, integrating infrared observations from different satellite systems. In detail, we combined SEVIRI data (3 km spatial resolution) with those from the polar-orbiting sensors AVHRR (1 km), VIIRS (350 m), MSI (20 m), and OLI (30 m), having a higher spatial resolution but a lower temporal sampling. This data integration allowed us to infer information about the different phases of the Stromboli eruption. Moreover, based on the mean silica content of 49.155 wt%, typical for low-porphyritic (LP) volatile-rich magma, which erupted during July/August 2019 at Stromboli, we estimated a mean output rate of 1.26 ± 0.63 m^3/s for this period, which is higher than the ones in the 2002–2003 and 2014 effusive eruptions, but is lower than in the 2007 eruption. During the two-months-long eruption period in July/August 2019, we estimated an erupted lava volume of $6.33 \times 10^6 \pm 3.17 \times 10^6$ m^3. This eruption was also characterized by the absence of lateral vents, while it showed a significant increase in frequency and energy of the Strombolian activity to the summit craters of the volcano, following a trend initiated after the 2007 eruption, probably due to the formation of a wider and warmer uppermost central conduit.

Author Contributions: S.P. designed the experiment, performed the analysis of the Sentinel-2/Landsat-8 data and the VIIRS data-based TADR estimation, and wrote the major parts of the paper. F.M. and N.P. performed the analysis of the AVHRR data. C.F. investigated the SEVIRI data. M.N. (Marco Neri) supported the volcanological analysis. F.M., N.P., C.F. and M.N. (Marco Neri) wrote the corresponding parts of the paper. M.N. (Michael Nolde) and S.M. supported the study and provided suggestions for its improvement. All authors reviewed the manuscript.

Funding: This research received no external funding.

Acknowledgments: MSG-SEVIRI data used in this study follow the EUMETSAT data policy and were made available through the license released by the Meteorological Service of the Italian Military Aeronautics. Sentinel-2

data are available through the European Space Agency Copernicus open access hub (https://scihub.copernicus.eu/). Landsat-8 data are available at the USGS Earth Explorer (https://earthexplorer.usgs.gov/).

Conflicts of Interest: The authors declare no conflict of interest.

References

1. Bertagnini, A.; Roberto, A.; Pompilio, M. Paroxysmal activity at Stromboli: Lessons from the past. *Bull. Volcan.* **2011**, *73*, 1229–1243. [CrossRef]
2. Calvari, S.; Spampinato, L.; Bonaccorso, A.; Oppenheimer, C.; Rivalta, E.; Boschi, E. Lava effusion—A slow fuse for paroxysms at Stromboli volcano? *Earth Planet. Sci. Lett.* **2011**, *301*, 317–323. [CrossRef]
3. Ripepe, M.; Pistolesi, M.; Coppola, D.; Delle Donne, D.; Genco, R.; Lacanna, G.; Laiolo, M.; Marchetti, E.; Ulivieri, G.; Valade, S. Forecasting effusive dynamics and decompression rates by magma static model at open-vent volcanoes. *Sci. Rep.* **2017**, *7*, 3885. [CrossRef] [PubMed]
4. Neri, M.; Lanzafame, G.; Acocella, V. Dike emplacement and related hazard in volcanoes with sector collapse: The 2007 Stromboli eruption. *J. Geol. Soc. Lond.* **2008**, *165*, 883–886. [CrossRef]
5. Neri, M.; Lanzafame, G. Structural features of the 2007 Stromboli eruption. *J. Volcanol. Geotherm. Res.* **2009**, *182*, 137–144. [CrossRef]
6. Calvari, S.; Bonaccorso, A.; Madonia, P.; Neri, M.; Liuzzo, M.; Salerno, G.; Behncke, B.; Caltabiano, T.; Cristaldi, A.; Giuffrida, G.; et al. Major eruptive style changes induced by structural modifications of a shallow conduit system: The 2007–2012 Stromboli case. *Bull. Volcan.* **2014**, *76*, 841. [CrossRef]
7. Maramai, A.; Graziani, L.; Tinti, S. Tsunamis in the Aeolian Islands (southern Italy): A review. *Mar. Geol.* **2005**, *215*, 11–21. [CrossRef]
8. Rosi, M.; Pistolesi, M.; Bertagnini, A.; Landi, P.; Pompilio, M.; Di Roberto, A. Stromboli volcano, Aeolian Islands (Italy): Present eruptive activity and hazards. *Geol. Soc. Lond. Mem.* **2013**, *37*, 473–490. [CrossRef]
9. Calvari, S.; Spampinato, L.; Lodato, L.; Harris, A.J.; Patrick, M.R.; Dehn, J.; Burton, M.R.; Andronico, D. Chronology and complex volcanic processes during the 2002–2003 flank eruption at Stromboli volcano (Italy) reconstructed from direct observations and surveys with a handheld thermal camera. *J. Geophys. Res. Solid Earth* **2005**, *110*. [CrossRef]
10. Harris, A.J.L.; Swabey, S.E.J.; Higgins, J. Automated thresholding of active lavas using AVHRR data. *Int. J. Remote Sens.* **1995**, *16*, 3681–3686. [CrossRef]
11. Lodato, L.; Spampinato, L.; Harris, A.; Calvari, S.; Dehn, J.; Patrick, M. The morphology and evolution of the Stromboli 2002–2003 lava flow field: An example of a basaltic flow field emplaced on a steep slope. *Bull. Volcan.* **2007**, *69*, 661–679. [CrossRef]
12. Calvari, S.; Lodato, L.; Steffke, A.; Cristaldi, A.; Harris, A.J.; Spampinato, L.; Boschi, E. The 2007 Stromboli eruption: Event chronology and effusion rates using thermal infrared data. *J. Geophys. Res. Solid Earth* **2010**, *115*. [CrossRef]
13. Ripepe, M.; Marchetti, E.; Ulivieri, G. Infrasonic monitoring at Stromboli volcano during the 2003 effusive eruption: Insights on the explosive and degassing process of an open conduit system. *J. Geophys. Res. Solid Earth* **2007**, *112*. [CrossRef]
14. Ripepe, M.; Delle Donne, D.; Genco, R.; Maggio, G.; Pistolesi, M.; Marchetti, E.; Lacanna, G.; Ulivieri, G.; Poggi, P. Volcano seismicity and ground deformation unveil the gravity-driven magma discharge dynamics of a volcanic eruption. *Nat. Commun.* **2015**, *6*, 6998. [CrossRef] [PubMed]
15. Di Traglia, F.; Calvari, S.; D'Auria, L.; Nolesini, T.; Bonaccorso, A.; Fornaciai, A.; Esposito, A.; Cristaldi, A.; Favalli, M.; Casagli, N. The 2014 Effusive Eruption at Stromboli: New Insights from In Situ and Remote-Sensing Measurements. *Remote Sens.* **2018**, *10*, 2035. [CrossRef]
16. Francis, P.W.; Rothery, D.A. Using the Landsat Thematic Mapper to detect and monitor active volcanoes: An example from Lascar volcano, northern Chile. *Geology* **1987**, *15*, 614–617. [CrossRef]
17. Wright, R.; Flynn, L.P.; Harris, A.J.L. Evolution of lava flow-fields at Mount Etna, 27–28 October 1999, observed by Landsat 7 ETM+. *Bull. Volcan.* **2001**, *63*, 1–7. [CrossRef]
18. Kaneko, T.; Wooster, M.J.; Nakada, S. Exogenous and endogenous growth of the Unzen lava dome examined by satellite infrared image analysis. *J. Volcan. Geotherm. Res.* **2002**, *116*, 151–160. [CrossRef]
19. Oppenheimer, C.; Francis, P. Remote sensing of heat, lava and fumarole emissions from Erta'Ale volcano, Ethiopia. *Int. J. Remote Sens.* **1997**, *18*, 1661–1692. [CrossRef]

20. Harris, A.J.L.; Stevenson, D.S. Thermal observations of open degassing conduits and fumaroles at Stromboli and Vulcano using remotely-sensed data. *J. Volcan. Geotherm. Res.* **1997**, *76*, 175–198. [CrossRef]
21. Oppenheimer, C. Volcanological applications of meteorological satellites. *Int. J. Remote Sens.* **1998**, *19*, 2829–2864. [CrossRef]
22. Bonaccorso, A.; Bonforte, A.; Calvari, S.; Del Negro, C.; Di Grazia, G.; Ganci, G.; Neri, M.; Vicari, A.; Boschi, E. The initial phases of the 2008–9 Mt. Etna eruption: A multi-disciplinary approach for hazard assessment. *J. Geophys. Res.* **2011**, *116*, B03203. [CrossRef]
23. Wright, R. MODVOLC: 14 years of autonomous observations of effusive volcanism from space. In *Detecting, Modelling and Responding to Effusive Eruptions*; Harris, A.J.L., de Groeve, T., Garel, F., Carn, S.A., Eds.; Geological Society Special Publications: London, UK, 2016; Volume 426, pp. 23–54. [CrossRef]
24. Marchese, F.; Filizzola, C.; Genzano, N.; Mazzeo, G.; Pergola, N.; Tramutoli, V. Assessment and improvement of a Robust Satellite Technique (RST) for thermal monitoring of volcanoes. *Remote Sens. Environ.* **2011**, *115–116*, 1556–1563. [CrossRef]
25. Coppola, D.; Laiolo, M.; Cigolini, C.; Delle Donne, D.; Ripepe, M. Enhanced volcanic hot-spot detection using MODIS IR data: Results from the MIROVA system. In *Detecting, Modelling and Responding to Effusive Eruptions*; Harris, A.J.L., de Groeve, T., Garel, F., Carn, S.A., Eds.; Geological Society Special Publications: London, UK, 2016; Volume 426. [CrossRef]
26. AVA. ASTER Volcano Archive. Available online: https://ava.jpl.nasa.gov/about.php (accessed on 20 August 2019).
27. Reath, K.; Pritchard, M.E.; Moruzzi, S.; Alcott, A.; Coppola, D.; Pieri, D. The AVTOD (ASTER Volcanic Thermal Output Database) Latin America archive. *J. Volcan. Geotherm. Res.* **2019**, *376*, 62–75. [CrossRef]
28. Zakšek, K.; Hort, M.; Lorenz, E. Satellite and ground based thermal observation of the 2014 effusive eruption at Stromboli volcano. *Remote Sens.* **2015**, *7*, 17190–17211. [CrossRef]
29. Plank, S.; Nolde, M.; Richter, R.; Fischer, C.; Martinis, S.; Riedlinger, T.; Schoepfer, E.; Klein, D. Monitoring of the 2015 Villarrica volcano eruption by means of DLR's experimental TET-1 satellite. *Remote Sens.* **2018**, *10*, 1379. [CrossRef]
30. Harris, A.J.L. *Thermal Remote Sensing of Active Volcanoes—A User's Manual*; Cambridge University Press: Cambridge, UK, 2013. [CrossRef]
31. Harris, A.J.L.; de Groeve, T.; Garel, F.; Carn, S.A. (Eds.) *Detecting, Modelling and Responding to Effusive Eruptions*; Geological Society Special Publications: London, UK, 2016. [CrossRef]
32. Harris, A.J.L.; Dehn, J.; Calvari, S. Lava effusion rate definition and measurement: A review. *Bull. Volcan.* **2007**, *70*, 1–22. [CrossRef]
33. Harris, A.J.L.; Rowland, S.K. FLOWGO: A kinematic thermos-rheological model for lava flowing in a channel. *Bull. Volcan.* **2001**, *63*, 20–44. [CrossRef]
34. Ganci, G.A.; Vicari, A.; Cappello, A.; Del Negro, C. An emergent strategy for volcano hazard assessment: From thermal satellite monitoring to lava flow modelling. *Remote Sens. Environ.* **2012**, *119*, 197–207. [CrossRef]
35. Calvari, S.; Neri, M.; Pinkerton, H. Effusion rate estimations during the 1999 summit eruption on Mount Etna, and growth of two distinct lava flow fields. *J. Volcan. Geotherm. Res.* **2003**, *119*, 107–123. [CrossRef]
36. Poland, M.P. Time-averaged discharge rate of subaerial lava at Kīlauea Volcano, Hawai'i, measured from TanDEM-X interferometry: Implications for magma supply and storage during 2011–2013. *J. Geophys. Res. Solid Earth* **2014**, *119*, 5464–5481. [CrossRef]
37. Coppola, D.; Ripepe, M.; Laiolo, M.; Cigolini, C. Modelling satellite-derived magma discharge to explain caldera collapse. *Geology* **2017**, *45*, 523–526. [CrossRef]
38. Coppola, D.; Barsotti, S.; Cigolini, C.; Laiolo, G.M.; Pfeffer, M.A.; Ripepe, M. Monitoring the time-averaged discharge rates, volumes and emplacement style of large lava flows by using MIROVA system: The case of the 2014–2015 eruption at Holuhraun (Iceland). *Ann. Geophys.* **2018**, *61*. [CrossRef]
39. Walter, T.R.; Haghighi, M.H.; Schneider, F.M.; Coppola, D.; Motagh, M.; Saul, J.; Babeyko, A.; Dahm, T.; Troll, V.R.; Tilmann, F.; et al. Complex hazard cascade culminating in the Anak Krakatau sector collapse. *Nat. Commun.* **2019**, *10*. [CrossRef]
40. ESA Sentinel Online. Available online: https://sentinel.esa.int/web/sentinel/user-guides/sentinel-2-msi/resolutions (accessed on 15 October 2019).

41. Pergola, N.; Marchese, F.; Tramutoli, V.; Filizzola, C.; Ciampa, M. Advanced satellite technique for volcanic activity monitoring and early warning. *Ann. Geophys.* **2008**, *51*, 287–301. [CrossRef]
42. Higgins, J.; Harris, A. VAST: A program to locate and analyze volcanic thermal anomalies automatically from remotely sensed data. *Comput. Geosci.* **1997**, *23*, 627–645. [CrossRef]
43. Pergola, N.; Marchese, F.; Tramutoli, V. Automated detection of thermal features of active volcanoes by means of infrared AVHRR records. *Remote Sens. Environ.* **2004**, *93*, 311–327. [CrossRef]
44. Lombardo, V. AVHotRR: Near-real time routine for volcano monitoring using IR satellite data. In *Detecting, Modelling and Responding to Effusive Eruptions*; Harris, A.J.L., de Groeve, T., Garel, F., Carn, S.A., Eds.; Geological Society Special Publications: London, UK, 2016; Volume 426, pp. 73–92. [CrossRef]
45. Mia, M.; Fujimitsu, Y.; Nishijima, J. Thermal activity monitoring of an active volcano using Landsat 8/OLI-TIRS sensor images: A case study at the Aso volcanic area in southwest Japan. *Geosciences* **2017**, *7*, 118. [CrossRef]
46. Marchese, F.; Neri, M.; Falconieri, A.; Lacava, T.; Mazzeo, G.; Pergola, N.; Tramutoli, V. The Contribution of Multi-Sensor Infrared Satellite Observations to Monitor Mt. Etna (Italy) Activity during May to August 2016. *Remote Sens.* **2018**, *10*, 1948. [CrossRef]
47. Valade, S.; Ley, A.; Massimetti, F.; D'Hondt, O.; Laiolo, M.; Coppola, D.; Loibl, D.; Hellwich, O.; Walter, T.R. Towards Global Volcano Monitoring Using Multisensor Sentinel Missions and Artificial Intelligence: The MOUNTS Monitoring System. *Remote Sens.* **2019**, *11*, 1528. [CrossRef]
48. Richter, L.; Louis, J.; Berthelot, B. *Sentinel-2 MSI—Level 2A Products Algorithm Theoretical Basis*; S2PAD-ATBD-0001; German Aerospace Center (DLR): Oberpfaffenhofen, Germany; VEGA, 2011.
49. Fire-Information-for-Resource-Management-System (FIRMS). Available online: https://firms.modaps.eosdis.nasa.gov (accessed on 31 October 2019).
50. Schroeder, W.; Giglio, L. *Visible Infrared Imaging Radiometer Suite (VIIRS) 375 m Active Fire Detection and Characterization Algorithm Theoretical Basis Document*; University of Maryland: Washington, DC, USA, 2016.
51. VIIRS Cloud Mask. CLDMSK_L2_VIIRS_SNPP. Available online: https://ladsweb.modaps.eosdis.nasa.gov/missions-and-measurements/products/CLDMSK_L2_VIIRS_SNPP/ (accessed on 31 October 2019).
52. Tramutoli, V. Robust satellite techniques (RST) for natural and environmental hazards monitoring and mitigation: Theory and applications. In Proceedings of the 2007 International Workshop on the Analysis of Multi-temporal Remote Sensing Images, Provinciehuis Leuven, Belgium, 18–20 July 2007; pp. 1–6. [CrossRef]
53. Finkensieper, S.; Stengel, M.; Selbach, N.; Hollmann, R.; Werscheck, M.; Meirink, J.F. ICDR SEVIRI Clouds—Based on CLAAS-2 Methods, Satellite Application Facility on Climate Monitoring. 2018. Available online: https://wui.cmsaf.eu/safira/action/viewICDRDetails?acronym=CLAAS_V002_ICDR (accessed on 15 October 2019).
54. Pergola, N.; Coviello, I.; Filizzola, C.; Lacava, T.; Marchese, F.; Paciello, R.; Tramutoli, V. *A Review of RSTVOLC, an Original Algorithm for Automatic Detection and Near-Real-Time Monitoring of Volcanic Hotspots from Space*; Geological Society Special Publications: London, UK, 2016; Volume 426, pp. 55–72. [CrossRef]
55. Wooster, M.J.; Zhukov, B.; Oertel, D. Fire radiative energy for quantitative study of biomass burning: Derivation from the BIRD experimental satellite and comparison to MODIS fire products. *Remote Sens. Environ.* **2003**, *86*, 83–107. [CrossRef]
56. Coppola, D.; Laiolo, M.; Piscopo, D.; Cigolini, C. Rheological control on the radiant density of active lava flows and domes. *J. Volcan. Geotherm. Res.* **2013**, *249*, 39–48. [CrossRef]
57. Landi, P.; Corsaro, R.A.; Francalanci, L.; Civetta, L.; Miraglia, L.; Pompilio, K.; Tesoro, R. Magma dynamics during the 2007 Stromboli eruption (Aeolian Islands, Italy): Mineralogical, geochemical and isotopic data. *J. Volcan. Geotherm. Res.* **2009**, *182*, 255–268. [CrossRef]
58. Istituto Nazionale di Geofisica e Vulcanologia (INGV). The 3 July 2019 paroxysm of Stromboli and its activity during the following days. Available online: https://ingvvulcani.com/2019/07/15/the-3-july-2019-paroxysm-of-stromboli-and-its-activity-during-the-following-days/ (accessed on 15 July 2019).
59. Zanon, V.; Neri, M.; Pecora, E. Interpretation of data from the monitoring thermal camera: The case of Stromboli volcano (Aeolian Islands, Italy). *Geol. Mag.* **2009**, *146*, 591–601. [CrossRef]